J. Fluid Mech. (1997), *vol.* 338, *pp.* 299–315

Printed in the United Kingdom © 1997 Cambridge University Press

Collision of two deformable drops in shear flow

By M. LOEWENBERG[1] AND E. J. HINCH[2]

[1] Department of Chemical Engineering, Yale University, New Haven, CT 06520-8286, USA

[2] Department of Applied Mathematics and Theoretical Physics, University of Cambridge, Silver Street, Cambridge CB3 9EW, UK

(Received 9 September 1996)

A boundary integral formulation is used to investigate the interaction between a pair of deformable drops in a simple shear flow. The interactions do not promote appreciably the breakup of the drops. For certain ratios of the viscosities of the drops and the suspending fluid, the lubrication gap that separates the two drops can diminish rapidly in the extensional quadrant of the flow. Slight deformation endows the drops with an apparent short-range repulsive interaction: drop coalescence requires van der Waals attraction which was not included in this study. From the trajectories of different collisions, the self-diffusion coefficients that describe the cross-flow migration of the non-Brownian drops in a dilute sheared emulsion are obtained. The self-diffusivities are very anisotropic, depend strongly on the viscosity ratio, and depend modestly on the shear rate.

1. Introduction

Shear-induced self-diffusion of non-Brownian drops in emulsions is important because it facilitates mixing. In the production of specialized polymer blends, macroscopic properties such as the mechanical strength of the product rely on effective mixing of the emulsified melt to produce a uniform microstructure.

In the absence of interfacial tension, the drop size in an efficient mixing device will continuously decrease until Brownian motion can effectively homogenize the fine droplets throughout the continuous phase. However, interfacial tension places a lower bound on the drop size that can be obtained by mixing. For drops in shear flow, significant deformation and breakup generally occur when the capillary number, $Ca = \mu\dot{\gamma}a/\sigma$ is $O(1)$, where $\dot{\gamma}$ is the imposed shear rate, a is the undeformed drop radius, μ is the continuous-phase viscosity, and σ is the interfacial tension. The numerical value of the critical capillary number depends on the dispersed-phase volume fraction ϕ and the ratio of the viscosities of the dispersed and continuous phases, λ.

For isolated drops with $0 < \lambda < 4$, the criterion $Ca = O(1)$ provides a reasonable estimate of the drop size produced by a given shear rate; for λ outside this range, isolated drops do not break in steady shear flow (Hinch & Acrivos 1980; Grace 1971). The effect of drop interactions on the critical capillary number has not been studied; thus the effect of volume fraction is unknown. The coalescence rate of undeformed spherical drops has been computed (Zinchenko 1984; Wang, Zinchenko & Davis 1994) but little is known about the tendency for deformable drops to coalesce.

Brownian motion of the drops produced by breakup at a given shear rate will be significant only if the Péclet number, $Pe = \mu\dot{\gamma}a^3/kT \leqslant O(1)$. If the shear rate is maintained, $Ca = O(1)$ and $Pe = O(\sigma a^2/kT)$. Given that surface tension results

https://doi.org/10.1017/S0022112097005016 Published online by Cambridge University Press

from molecular interactions (e.g. disjoining pressure), we estimate $\sigma \sim kT/b^2$, where $b \ll a$ is a molecular length scale. Thus, $Pe \gg 1$ under typical conditions, so that Brownian motion is unimportant. Moreover, $Pe \leqslant O(1)$ and $Ca = O(1)$ imply that $\dot{\gamma} \geqslant \sigma^{3/2}/\mu(kT)^{1/2}$. These conditions are rarely attained in practice either because the volumetric power, $\sigma^3/\mu kT$, is unavailable or because the resultant viscous heating would be detrimental. Typical mixing operations generate non-Brownian deformable drops characterized by $Pe \gg 1$ and $Ca = O(1)$. Thus, self-diffusion of deformable drops is an essential mixing mechanism in most emulsification processes.

The $O(a)$ displacements and $O(\dot{\gamma}a)$ relative velocities between interacting particles or drops produce self-diffusivities that are $O(\dot{\gamma}a^2)$. Cross-flow self-diffusion of smooth spheres can only result from multi-particle interactions because pairwise interactions cannot generate a net cross-flow displacement. Shear-induced self-diffusion of rigid spherical particles has been experimentally observed (Eckstein, Bailey & Shapiro 1977; Leighton & Acrivos 1987) and numerically simulated (Brady & Bossis 1987). Wang, Mauri & Acrivos (1996) calculated the small $O(\phi^2\dot{\gamma}a^2)$ cross-flow self-diffusivity in a sheared dilute suspension of smooth spheres.

Pairwise interactions can induce larger $O(\phi\dot{\gamma}a^2)$ self-diffusivities in dilute suspensions of nonspherical or deformable particles or particles that are stabilized against aggregation by a repulsive interaction. da Cunha & Hinch (1996) computed the self-diffusivity of rough spheres in a dilute suspension. However, there have been no studies on the self-diffusion of drops.

The primary aim of this article is to compute cross-flow self-diffusion coefficients of non-Brownian deformable drops in a sheared dilute emulsion. The tendency for interacting deformable drops to break up and coalesce in shear flow are related issues. The effects of the capillary number and viscosity ratio are the focus of our study. Neutrally buoyant drops and a monodisperse drop size distribution are assumed. Marangoni stresses on the drop interfaces that result from surfactant concentration gradients are neglected. Low-Reynolds-number conditions are assumed which restricts practical application of our results for $Ca = O(1)$ to suspending fluids that are about 100 times more viscous than water.

In §2, the numerical procedures are described. Numerical results describing the trajectories and near-contact motion of a pair interacting drops are presented in §3; self-diffusion coefficients are presented in §4. Concluding remarks are made in §5.

2. Calculation procedure

2.1. *Interactions between deformable drops*

Boundary integral calculations were used to compute the interactions and trajectories of deformable drops ($Ca > 0$) in shear flow as sketched in figure 1. Following Loewenberg & Hinch (1996) each drop interface, S_1 and S_2, was discretized into N flat triangular elements and the velocity was computed at collocation points $\boldsymbol{x}$ on the interfaces using the multidrop non-singular boundary integral formulation:

$$
\begin{aligned}
(\lambda+1)\boldsymbol{u}(\boldsymbol{x}) &= 2x_2 + (\lambda-1)\boldsymbol{u}(\boldsymbol{x}) \\
&-\frac{1}{4\pi}\int_{S_1(\boldsymbol{x}')}\left[\frac{1}{Ca}\left[\kappa(\boldsymbol{x}')-\kappa(\boldsymbol{x}^*)\right]\boldsymbol{G}(\widehat{\boldsymbol{x}})\cdot\boldsymbol{n}(\boldsymbol{x}') + (\lambda-1)\left[\boldsymbol{u}(\boldsymbol{x}')-\boldsymbol{u}(\boldsymbol{x}^*)\right]\cdot\boldsymbol{T}(\widehat{\boldsymbol{x}})\cdot\boldsymbol{n}(\boldsymbol{x}')\right]\mathrm{d}\boldsymbol{x}' \\
&-\frac{1}{4\pi}\int_{S_2(\boldsymbol{x}')}\left[\frac{1}{Ca}\left[\kappa(\boldsymbol{x}')-\kappa(\boldsymbol{x}^*)\right]\boldsymbol{G}(\widehat{\boldsymbol{x}})\cdot\boldsymbol{n}(\boldsymbol{x}') + (\lambda-1)\left[\boldsymbol{u}(\boldsymbol{x}')-\boldsymbol{u}(\boldsymbol{x}^*)\right]\cdot\boldsymbol{T}(\widehat{\boldsymbol{x}})\cdot\boldsymbol{n}(\boldsymbol{x}')\right]\mathrm{d}\boldsymbol{x}',
\end{aligned}
\tag{2.1}
$$

https://doi.org/10.1017/S0022112097005016 Published online by Cambridge University Press

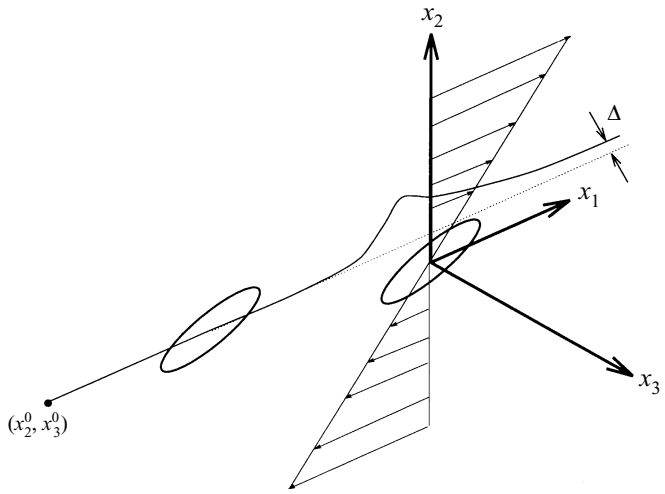


FIGURE 1. Schematic of the relative trajectory between a pair of deformable interacting drops in shear flow.

which was made dimensionless using a and $\dot{\gamma}a$ for the characteristic length and velocity; x_2 is the dimensionless imposed shear flow shown in figure 1. The local mean curvature κ and the outward normal vector $\boldsymbol{n}$ on the drop surfaces were obtained by line integration (Loewenberg & Hinch 1996). The Stokeslet and stresslet are

$$\boldsymbol{G} = \frac{\boldsymbol{I}}{r} + \frac{\widehat{\boldsymbol{x}}\widehat{\boldsymbol{x}}}{r^3} \text{ and } \boldsymbol{T} = -6\frac{\widehat{\boldsymbol{x}}\widehat{\boldsymbol{x}}\widehat{\boldsymbol{x}}}{r^5},$$

where $\widehat{\boldsymbol{x}} = \boldsymbol{x}' - \boldsymbol{x}$ and $r = |\,\widehat{\boldsymbol{x}}\,|$. The formulation is rendered non-singular by taking $\boldsymbol{x}^*$ as the collocation point closest to $\boldsymbol{x}$ (Loewenberg & Hinch 1996).

The non-singular surface integrals in (2.1) were evaluated with integrand evaluations only at the collocation points and the contribution from the boundary element containing $\boldsymbol{x}$ was excluded. Errors introduced by the curvature calculation dominate the $O(N^{-1})$ errors introduced by this simple integration rule and the use of flat triangular boundary elements (Loewenberg & Hinch 1996). Equation (2.1) was solved by Picard iteration, inserting velocities from the last iteration back into the equation. Eigensolution purging (Pozrikidis 1992, pp. 120–127) was used to accelerate iterative convergence and enable calculations with $\lambda \ll 1$ and $\lambda \gg 1$. Adequate pointwise convergence was obtained with only a few iterations. For the special case $\lambda = 1$, equation (2.1) provides an explicit formula for $\boldsymbol{u}(\boldsymbol{x})$.

2.2. *Trajectories of deformable drops*

Trajectories of deformable drops were computed by advancing the collocation points on the drop surfaces according to the kinematical condition:

$$\frac{\mathrm{d}\boldsymbol{x}}{\mathrm{d}t} = \boldsymbol{u}(\boldsymbol{x}) + \boldsymbol{w}(\boldsymbol{x}), \tag{2.2}$$

where $\boldsymbol{u}(\boldsymbol{x})$ is the actual velocity of the collocation point obtained by solving (2.1) and $\boldsymbol{w}(\boldsymbol{x})$ is a locally defined tangential 'velocity' field that maintains a desirable distribution of collocation points on the drop surfaces with a somewhat higher density of points in the near-contact region between the drops and on regions with high curvature. The precise local rule that defines $\boldsymbol{w}$ is unimportant; in all cases,

https://doi.org/10.1017/S0022112097005016 Published online by Cambridge University Press

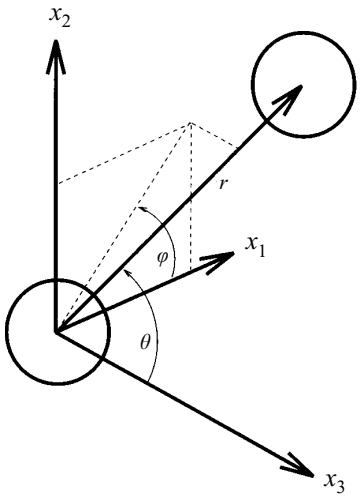


FIGURE 2. Schematic of coordinate system for describing the interaction between spherical drops.

a well-controlled grid of collocation points was maintained with the rule used by Loewenberg & Hinch (1996).

Equation (2.2) was integrated using a second-order Runge–Kutta scheme with time steps, $\Delta t = \frac{1}{2}Ca\Delta x$, where $\Delta x = O(N^{-1/2})$ is the minimum separation between the collocation points on a drop interface (Rallison 1981). Our results were unaffected by smaller time steps and were unstable for larger steps. The $O(N^{-1})$ time integration error of this procedure is the same order as the surface integration errors and smaller than the curvature calculation errors (Loewenberg & Hinch 1996).

2.3. *Trajectories of spherical drops*

For the limiting case $Ca \to 0$, spherical drop trajectories were obtained by second-order Runge–Kutta integration of the differential equations:

$$\frac{\mathrm{d}r}{\mathrm{d}t} = \tfrac{1}{2}\,[1 - A(r,\lambda)]\, r \sin^2\theta \sin 2\varphi\ , \tag{2.3a}$$

$$\frac{\mathrm{d}\theta}{\mathrm{d}t} = \tfrac{1}{4}\,[1 - B(r,\lambda)] \sin 2\theta \sin 2\varphi\ , \tag{2.3b}$$

$$\frac{\mathrm{d}\varphi}{\mathrm{d}t} = -\sin^2\varphi - \tfrac{1}{2}B(r,\lambda)\cos 2\varphi\ , \tag{2.3c}$$

where the coordinates are defined in figure 2 and the variables have been made dimensionless using a and $\dot{\gamma}^{-1}$ for the characteristic length and time; three-decimal-place convergence was obtained with $\Delta t = 10^{-3}$. The mobility functions, $A(r,\lambda)$ and $B(r,\lambda)$, describe the interactions between spherical drops in a linear flow field. For near-contact motion $r \to 2$, $A \to 1$ and B tends to a positive constant less than unity; both functions vanish at large separations $r \to \infty$. At all separations, $B(r,0) = 0$. The near- and far-field asymptotic behaviour of these functions has been derived and a bispherical coordinate solution has been obtained (Zinckenko 1982, 1983). Herein, the mobility functions were evaluated with Zinchenko's FORTRAN subroutines (personal communication).

https://doi.org/10.1017/S0022112097005016 Published online by Cambridge University Press

2.4. *Self-diffusivities*

The self-diffusion tensor is defined as half the rate-of-change of the random walk variance:

$$\boldsymbol{D} = \lim_{t\to\infty} \frac{1}{2}\frac{\mathrm{d}}{\mathrm{d}t}\langle \boldsymbol{\Delta}\boldsymbol{\Delta}\rangle \quad , \tag{2.4}$$

where the cross-flow random walk displacement, $\boldsymbol{\Delta}$, has zero mean. The cross-flow displacement, $\boldsymbol{\Delta} = (\Delta_2, \Delta_3)$, is defined in figure 1. For given values of Ca and λ, the cross-flow displacement of a drop resulting from its pairwise interaction with another identical drop depends on the initial offset of the drop trajectories, (x_2^0, x_3^0), at large separations in the flow direction, x_1. Only uncorrelated pairwise interactions between identical drops are considered on the assumption that the emulsion is dilute and monodisperse.

The rate of interactions that result in a particular cross-flow displacement, $\boldsymbol{\Delta}(x_2^0, x_3^0; Ca, \lambda)$, is $n\dot{\gamma}\,|x_2^0|\,\mathrm{d}x_2^0\,\mathrm{d}x_3^0$, where n is the number density of drops: $\phi = \frac{4}{3}\pi a^3 n$. By definition (2.4), the dimensionless self-diffusion coefficient for a dilute emulsion is (da Cunha & Hinch 1996)

$$f_\alpha(Ca, \lambda) = \frac{D_\alpha}{\phi\dot{\gamma}a^2} = \frac{3}{2\pi}\int_0^\infty \int_0^\infty \Delta_\alpha^2 x_2^0 \;\; \mathrm{d}x_2^0 \mathrm{d}x_3^0 \quad , \tag{2.5}$$

where $\alpha = 2$ or 3 for cross-flow self-diffusion in the velocity gradient or the vorticity direction (cf. figure 1). The result exploits the four-fold symmetry of integration in the (x_2^0, x_3^0)-plane.

For deformable drops, the double integral of formula (2.5) was evaluated using integrand values on the truncated square domain, $(x_2^0, x_3^0) \in [0, X_2] \times [0, X_2]$ with $\boldsymbol{\Delta}(x_2^0, x_3^0)$ obtained by integrating (2.2). For widely separated neutrally-buoyant drops, the cross-flow velocity is $\dot{\boldsymbol{\Delta}} \sim R/r^3$, where $r \approx (R^2 + x_1^2)^{1/2} \gg 1$ is the drop separation, x_1 is the component of separation in the flow direction, and $R = [(x_2^0)^2 + (x_3^0)^2]^{1/2}$ is the initial cross-flow separation. Using $\dot{x}_1 \sim R$, we obtain $\mathrm{d}\Delta/\mathrm{d}x_1 \sim 1/r^3$. Then integrating from zero to infinity, we obtain the estimate $\Delta(x_2^0, x_3^0) \sim R^{-2}$ for $R \gg 1$. Thus, the domain truncation error for the double integral of formula (2.5) is $O(X_2^{-1})$.

Using the asymptotic form derived above, we extrapolated our results to obtain a smaller $O(X_2^{-2})$ domain truncation error. For deformable drops, the calculations presented herein were obtained with an $X_2 = 4$ domain truncation. A comparison between the values obtained with $X_2 = 4$ and $X_2 = 8$ indicate that the domain truncation error is 1–2%. On the inner portion of the truncated integration domain, $(x_2^0, x_3^0) \in [0, 2] \times [0, 2]$, a two-dimensional Simpson's rule was implemented on a 5×5 rectangular mesh; a trapezoid rule with a coarser 5×5 mesh was used on the remainder of the truncated region, where the integrand is smaller and slowly varying. This integration procedure requires 32 trajectory calculations and is accurate to about 1% for integrands similar to that in (2.5).

Unstabilized hydrodynamically interacting spherical drops will coalesce for $R \leqslant 2E_{12}^{1/3}$, where E_{12} is the 'collision efficiency' (Wang *et al.* 1994); for equal-size spherical drops with $\lambda = 1$, $E_{12} = 0.38$. Herein, spherical drops were stabilized against coalescence by supplementing (2.3) with a singular, infinitesimally short-range repulsion described by setting $A = 1$ for $0 < r - 2 < \delta$ in the compressive quadrant of the flow field, $\varphi > \pi/2$ (Zinchenko 1984). In general, the results depend on the value of δ but for $\delta < 10^{-4}$ our results, accurate to three digits, were insensi-

https://doi.org/10.1017/S0022112097005016 Published online by Cambridge University Press

tive to δ. For spherical drops with short-range repulsion, $\mathbf{\Delta}(x_2^0, x_3^0)$ is non-zero only within the circular domain $R \leqslant 2E_{12}^{1/3}$ and it was evaluated by integrating (2.3). The mobility functions were tabulated for improved computational speed. Formula (2.5) was evaluated using a trapezoid rule with a 40×40 rectangular grid on the domain $(x_2^0, x_3^0) \in \left[0, 2E_{12}^{1/3}\right] \times \left[0, 2E_{12}^{1/3}\right]$. Results obtained with courser grids indicate that the integration error is about 0.1%.

Deformable drops can also be stabilized with a short-range repulsive interaction (Loewenberg & Hinch 1996); however, this was implemented only for $2 \leqslant \lambda \leqslant 5$ and for $\lambda < 0.1$ on the most closely spaced trajectories ($R < 1$). As explained in §3.2, very small surface separations occur under these conditions. For $\lambda = 1$, we confirmed that the short-range repulsion had a negligible effect on the drop trajectories. Calculations for closely spaced trajectories with $Ca < 0.1$ are impractical because of the exceedingly small surface separations that occur.

Cross-flow trajectory offsets were obtained with one drop initially centred at the origin and the second initially at a downstream location, $(-X_1, x_2^0, x_3^0)$. Trajectory integration was continued until the second drop passed the plane $x_1 = +X_1$. For deformable drops, the initial drop shapes corresponded to the stationary shapes of isolated drops under the same flow conditions. The error induced by trajectory truncation is $O(X_1^{-3})$. We used $X_1 = 8$ for deformable drops and $X_1 = 20$ for spherical drops. Based on a limited number of calculations with larger values of X_1, we estimate that trajectory truncation error is about 1% for deformable drops and about 0.1% for spherical drops. Trajectory truncation errors could be reduced by analytically integrating the far-field form of the pair interaction on the trajectory tails, $|x_1| > X_1$; however, errors induced elsewhere in the calculation procedure do not warrant this refinement.

2.5. *Computation time and numerical convergence*

For deformable drops, the computation time is dominated by the $O(N^2)$ integrand evaluations needed for the surface integrals in (2.1) at each time step. Given that $\Delta t \sim CaN^{-1/2}$, the total CPU time required to compute the self-diffusion tensor is $O(N^{5/2}Ca^{-1})$. For $N = 720$, $\Delta t \simeq 0.06\ Ca$ and for $\lambda = 1$ a time step requires 0.36 CPU seconds on a Hewlett-Packard 9000 series 735 workstation with the standard optimizing FORTRAN compiler. Depending on the trajectory offset, a complete trajectory requires about 3 CPU minutes for $Ca = 0.3$ and $\lambda = 1$; self-diffusion coefficients were obtained in 2 CPU hours. The calculations are 3–4 times slower for $\lambda \neq 1$ because (2.1) must be solved by iteration.

The results depicted in figure 3 demonstrate numerical convergence of the boundary integral calculations for trajectories of deformable drops. Loewenberg & Hinch (1996) showed that curvature values have only $O(N^{-1/2})$ pointwise accuracy but that integrals of the curvature over large portions of a drop interface are accurate to $O(N^{-1})$. Figure 3(*b*) demonstrates that the total discretization error resulting from the curvature calculation, surface integration, and trajectory integration is $O(N^{-1})$. Herein, self-diffusivities were computed with $N = 720$; discretization errors are therefore about 2% according to figure 3(*b*) which is comparable to the remaining sources of error discussed in §2.4.

Self-diffusivities for spherical drops require less than a minute of CPU time and are accurate to about 0.1%.

https://doi.org/10.1017/S0022112097005016 Published online by Cambridge University Press

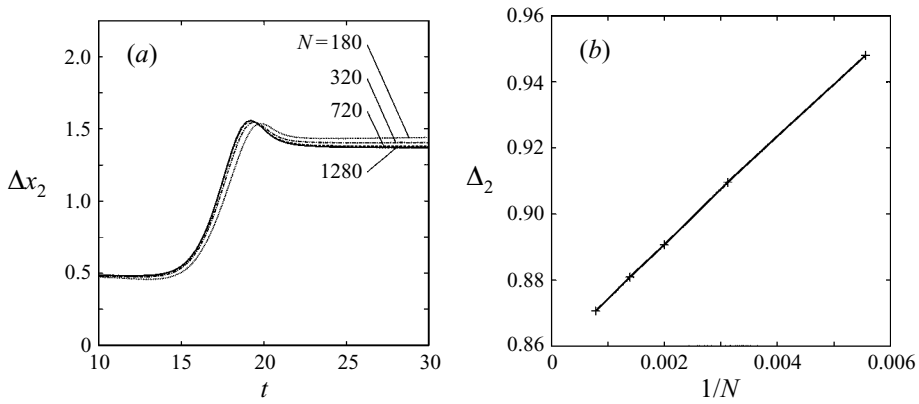


FIGURE 3. Relative trajectory of two interacting drops for $Ca = 0.3$, $\lambda = 1$; initially, one drop centred at the origin, second drop at $(-10, 0.5, 0)$. (*a*) Cross-flow separation (velocity gradient direction) versus time; results obtained obtained using $N = 180$ (dotted curve), 320 (dashed-dotted curve), 720 (dashed curve), and 1280 (solid curve) boundary elements. (*b*) Cross-flow displacement versus reciprocal number of boundary elements, $1/N$.

3. Numerical results

3.1. *Drop trajectories*

The trajectories depicted in figures 4 and 6 illustrate how pairwise interactions between drops are affected by the shear rate (capillary number) and the drop viscosity. Figures 5 and 7 show the corresponding trajectory offsets that occur during the interactions. The initial conditions, given in the captions of figures 4 and 6, are the same for all trajectories. The capillary number is the ratio of the distorting viscous stresses, $\mu\dot{\gamma}$, to the restoring stress of surface tension, σ/a; thus, drop deformation increases with Ca as illustrated in figure 4. The drop rotation rate is $\dot{\gamma}$ and the drop relaxation rate is $\sigma/[\mu a(1+\lambda)]$; thus, drop deformation decreases with drop viscosity, as shown in figure 6.

3.2. *Near-contact motion: approach of drops*

In this subsection, we present scaling arguments that predict the area of the near-contact region between closely spaced drops that are pressed together in shear flow and the thinning rate of the film that separates their surfaces. The arguments implicitly assume that the duration of close interaction scales with the inverse shear rate which is insufficient to form a dimpled near-contact region. The trajectories shown in figures 5 and 7 support this estimate of the interaction time and near-contact dimpling is not seen for the results depicted in figures 4 and 6.

A thin film with thickness h and lateral extent $d \gg h$ forms between drops that are pressed together in the compressional quadrant of a shear flow by a viscous force, $\mu\dot{\gamma}a^2$. The lateral extent of the near-contact region depends on Ca and λ as shown in table 1. For the smallest capillary numbers, the lateral scaling is based on the geometry of a sphere. In the intermediate range, d is obtained from a force balance with capillary pressure balancing the lubrication pressure in the near-contact region: $\sigma/a \sim \mu\dot{\gamma}a^2/d^2$; for $Ca = O(1)$, this yields $d \sim aCa^{1/2}$. For $\lambda \gg 1$ and $Ca \geqslant \lambda^{-2/3}$, this balance cannot be achieved during the drop interaction time, $\dot{\gamma}^{-1}$. Instead, the lateral scaling for very viscous drops is obtained by equating the pressure in the near-contact region to the viscous stress that resists deformation, $\mu\lambda\dot{\delta}/d$, where δ is the depression of the drop interface in the near-contact region. Thus, $\dot{\delta}$ is the characteristic velocity

https://doi.org/10.1017/S0022112097005016 Published online by Cambridge University Press

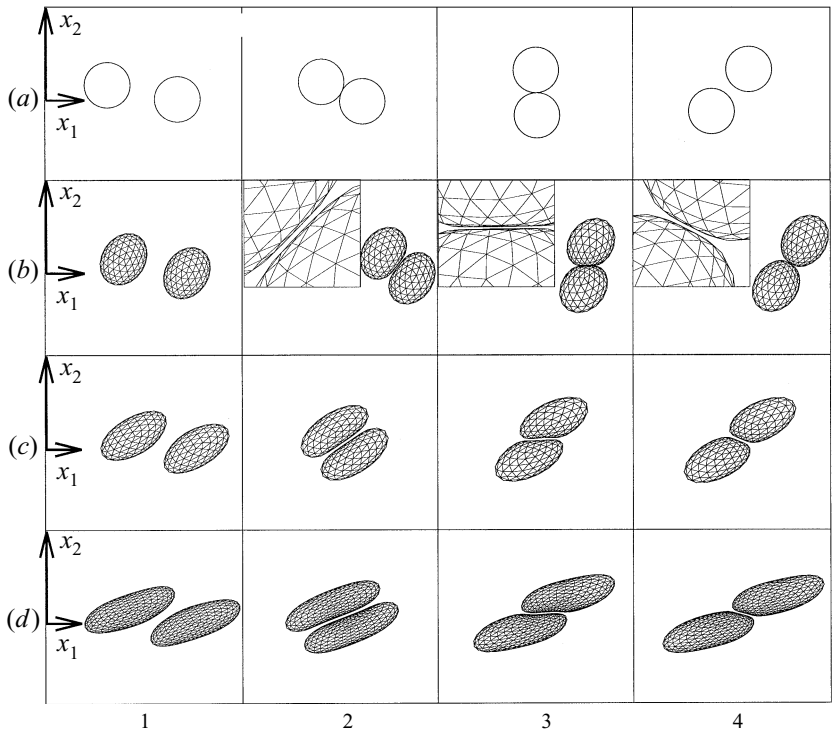


FIGURE 4. Sequences (1–4) showing the interactions between two drops in shear flow with $\lambda = 1$: (*a*) $Ca = 0$, (*b*) $Ca = 0.1$, (*c*) $Ca = 0.3$, (*d*) $Ca = 0.4$. Insets show magnified view of near-contact region. Initially, one drop is centred at the origin, the other at $(-10, 0.5, 0)$. Initially, each drop has the steady shape of an isolated drop under same flow conditions.

$Ca \ll h/a$	$h/a \leqslant Ca \ll (1+\lambda)^{-2/3}$	$Ca = O(1+\lambda)^{-2/3}$
$d \sim (ha)^{1/2}$	$d \sim aCa^{1/2}$	$d \sim a(1+\lambda)^{-1/3}$

TABLE 1. Lateral extent of the near-contact region between drops.

inside the drops where the viscosity is $\mu\lambda$; variations in the internal velocity occur on the length scale d. Then taking $\delta \sim d^2/a$ yields $d^2\dot{d} \sim \dot{\gamma}a^3/\lambda$ which is integrated over the time of drop interaction to obtain $d \sim a\lambda^{-1/3}$. This physical description is analogous to that of elastic particles – replacing the viscous stress by the elastic stress $v\delta/d$, where v is the appropriate elastic modulus, we recover the contact area, $d^2 \sim a^2\left(\mu\dot{\gamma}/v\right)^{2/3}$.

The local velocity in the near-contact region between two drops is $u = u_p + u_t$, where u_t is the tangential velocity on the drop interfaces and

$$u_p = -\frac{1}{2\mu}\frac{\mathrm{d}p}{\mathrm{d}r}z\,(h-z)$$

is the pressure-driven flow. In the absence of Marangoni stresses, the tangential stress is continuous across the drop interface, thus

$$\mu\frac{u_p}{h} \sim \mu\lambda\frac{u_t}{d}.$$

https://doi.org/10.1017/S0022112097005016 Published online by Cambridge University Press

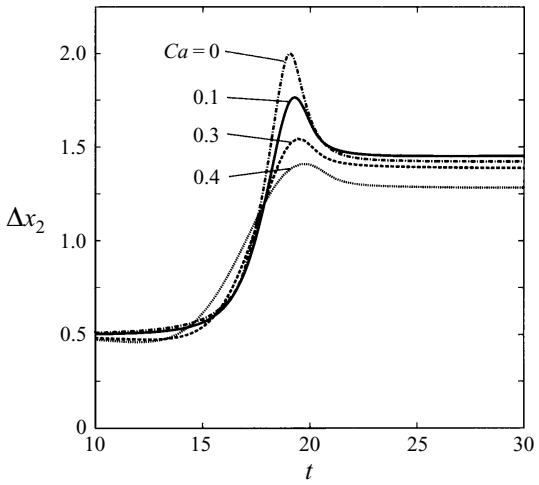


FIGURE 5. Cross-flow separation (velocity gradient direction) versus time between interacting drops with the capillary numbers indicated and $\lambda = 1$. Results correspond to sequences depicted in figure 4.

From mass continuity, $d^2\dot{h} \sim -hd\,(u_p + u_t)$, it follows that

$$\frac{\dot{h}}{h} \sim -\frac{u_p}{\lambda d}\left(\lambda + \frac{d}{h}\right).$$

Then taking

$$u_p \sim \frac{\Delta p}{\mu}\frac{h^2}{d},$$

where $\Delta p \sim \mu\dot{\gamma}a^2/d^2$ is the pressure in the near-contact region, we obtain the predicted approach rate

$$\left(\frac{\dot{h}}{h}\right)_{\mathrm{APP}} \sim -\dot{\gamma}\frac{h^2a^2}{d^4}\left(1 + \frac{d}{\lambda h}\right), \qquad \text{for} \qquad \lambda > \frac{h^2a}{d^3}. \tag{3.1}$$

The foregoing derivation relies on the assumption that the pressure in the near-contact region dominates stresses on the remainder of the drop surfaces which requires that $\mu a\dot{h} < \Delta p d^2$. This condition is not satisfied for very low drop viscosities $\lambda \leqslant h^2a/d^3$.

For $d/\lambda h \gg 1$, the flow in the near-contact region is dominated by the uniform flow u_t and the lubrication resistance is dominated by the flow within the drops; the drop interfaces are 'fully mobile'. In the complementary regime for highly viscous drops, u_p dominates the flow in the near-contact region and gives rise to the lubrication resistance.

For spherical drops, $Ca \ll h/a$ where $d \sim (ha)^{1/2}$, an initial gap h_0 will decrease as

$$h/h_0 \sim \left(1 - \frac{\dot{\gamma}t}{\lambda}(a/h_0)^{1/2}\right)^2$$

for $\lambda < d/h$ and thus predicts that coalescence can occur (Davis, Schonberg & Rallison 1989). For $\lambda > d/h$, $h = h_0\exp(-\dot{\gamma}t)$ indicating that coalescence is prevented or delayed until $h < d/\lambda$. Figure 4(*a*) shows that stabilized spherical drops with $\lambda = 1$ make apparent contact (frame 2) then rotate and slide according to (2.3) with $A = 1$.

https://doi.org/10.1017/S0022112097005016 Published online by Cambridge University Press

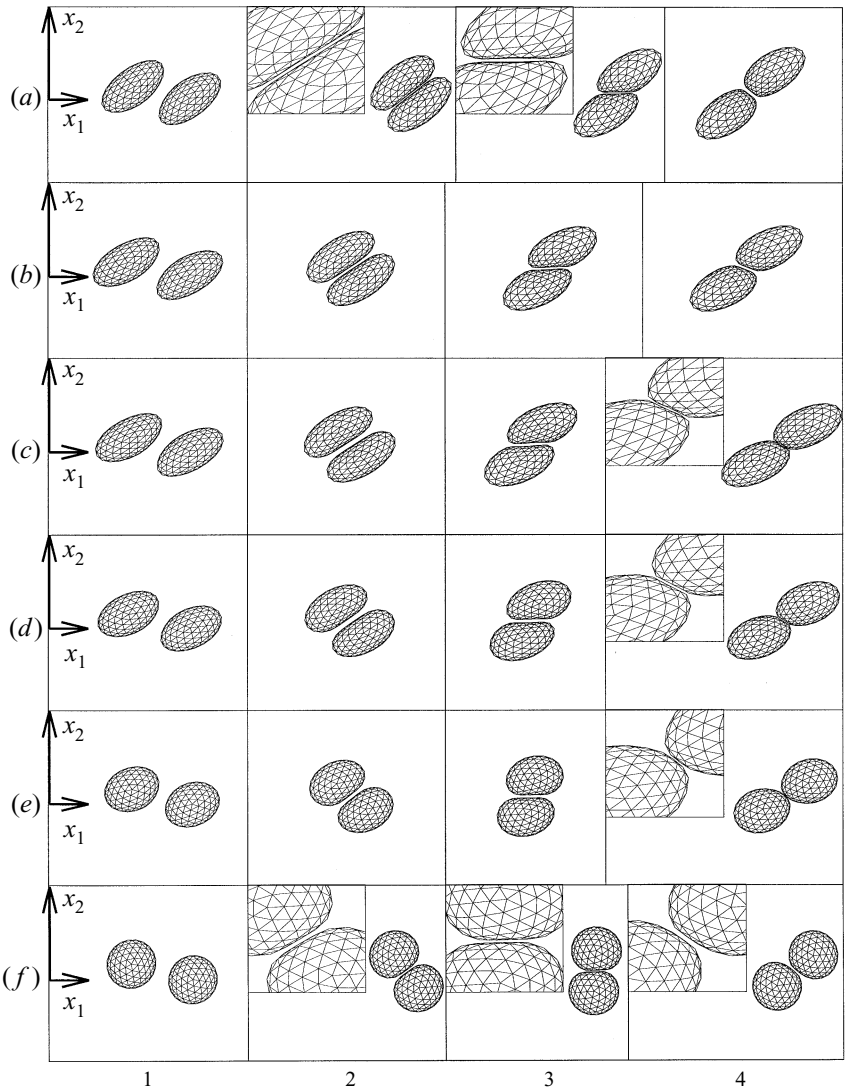


FIGURE 6. Sequences (1–4) showing the interactions between two drops in shear flow with $Ca = 0.3$: (*a*) $\lambda = 0.25$, (*b*) $\lambda = 1$, (*c*) $\lambda = 2$, (*d*) $\lambda = 4$, (*e*) $\lambda = 8$, (*f*) $\lambda = 20$. Insets show magnified view of near-contact region. Initially, one drop is centred at the origin, the other at $(-10, 0.5, 0)$. Initially, each drop has the steady shape of an isolated drop under same flow conditions.

When $\varphi = \pi/2$ (frame 3), the drops again separate. Unstabilized spherical drops would coalesce on this trajectory.

For $Ca > 0$, d becomes independent of h as $h \to 0$ so that (3.1) predicts slow algebraic film thinning: $h/a \sim (\lambda/\dot{\gamma}t)(d/a)^3$ thus, a non-hydrodynamic singular force such as van der Waals attraction is required for drop coalescence. This prediction is demonstrated by the trajectories depicted in figures 4 and 6; calculations with smaller initial offsets further confirm this observation. This conclusion is consistent with the results of Yiantsios & Davis (1991) for buoyancy-driven motion with $Ca \ll 1$.

For slightly deformable drops $h/a \leqslant Ca \ll (1+\lambda)^{-2/3}$, the film thinning rate decreases with capillary number. An estimate for the gap thickness separating two

https://doi.org/10.1017/S0022112097005016 Published online by Cambridge University Press

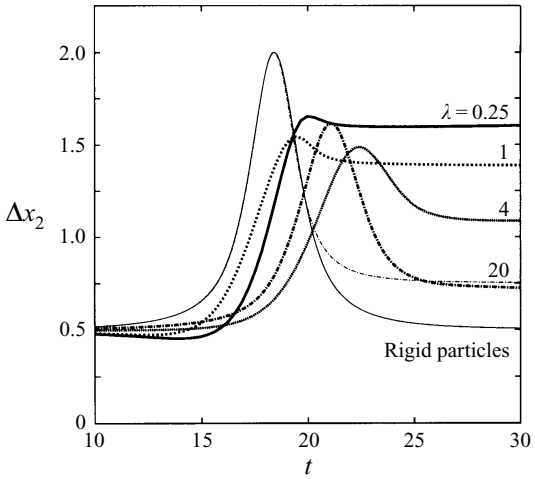


FIGURE 7. Cross-flow separation (velocity gradient direction) versus time between interacting drops with the viscosity ratios indicated. Thick curves correspond to sequences shown in figure 6 with $Ca = 0.3$ (trajectory for $\lambda = 8$ omitted for clarity). Fine solid curve: trajectory for smooth rigid spheres; fine dash-dotted curve: $Ca = 0$, $\lambda = 20$.

drops after they pass through the compressional quadrant of a shear flow is obtained by integrating (3.1) over the drop interaction time. Accordingly, $h/a \sim \lambda Ca^{3/2}$ for $\lambda \leqslant aCa^{1/2}/h$, and $h/a \sim Ca$ for highly viscous drops. Thus we predict the gap to increase with Ca, as the comparison of figures 4(b) and 4(c) illustrates, and increase with λ for $\lambda < d/h$, as shown in figure 6(a–c).

For $Ca = O(1)$ and $\lambda = O(1)$, integration of (3.1) indicates that the gap between two drops is $h/a \sim \lambda$. For highly viscous deformable drops $\lambda \geqslant (a/h)^{3/4}$, $h/a \sim \lambda^{-2/3}$ after the drops are pressed together in the compressional quadrant of the flow. For viscosities in the intermediate range $(a/h)^{3/4} \geqslant \lambda \gg 1$, the resistance to internal circulation increases with drop viscosity but the size of the lubrication region decreases with drop viscosity. These offsetting effects cancel so that film thickness is predicted to be independent of viscosity ratio. Figure 6 demonstrates that the film thickness after compression is insensitive to viscosity ratio in the range $2 \leqslant \lambda \leqslant 8$ under the conditions shown. For larger viscosities, the film thickness decreases with viscosity ratio as the comparison of figures 6(e) and 6(f) demonstrates.

3.3. *Near-contact motion: separation of drops*

In this subsection, we present scaling arguments for the separation of closely spaced deformable drops in shear flow.

In the extensional quadrant of the shear flow, the internal circulation $\hat{u}$ can be estimated by continuity of tangential stress on the drops: $\mu\dot{\gamma}a \sim \mu(1+\lambda)\hat{u}$. At the centre of the near-contact region, the internal flow vanishes by symmetry so that $\hat{u} \sim \dot{\gamma}d/(1+\lambda)$ in the near-contact region, where d is the lateral extent of the near-contact region that was formed when the drops passed through the compressive quadrant of the flow; the scaling for d is provided in table 1. The pressure associated with the internal flow is $\Delta\hat{p} \sim \mu\lambda\dot{\gamma}/(1+\lambda)$. The sense of this internal circulation draws fluid from the gap and thus tends to *reduce* the separation between the drops.

The velocity in the gap between the drops surfaces is $u = u_p + u_t$, where u_t is the tangential velocity on the drop interface and $u_p = (\Delta p/\mu)(h^2/d)$ is the pressure-

https://doi.org/10.1017/S0022112097005016 Published online by Cambridge University Press

driven flow. The normal stress balance on the drop interface is $\Delta p = \Delta\hat{p} - \kappa\sigma$, where $\kappa = O(1/a)$ is the local curvature of the interface. Suction in the gap cannot exceed the negative pressure induced by the flow, thus $\Delta p = \Delta\hat{p} - \min\left(\sigma/a, \mu\dot{\gamma}a^2/d^2\right)$. The tangential stress balance is $\mu\lambda\left(u_t - \hat{u}\right)/d = \mu u_p/h$. Putting together all of these relations, we obtain

$$u \sim \dot{\gamma}\left[\frac{d}{1+\lambda} - \frac{h^2a^2}{d^3}\frac{1+d/h\lambda}{1+Ca(a/d)^2}\right],$$

indicating that fluid can flow in or out of the gap between the drops. By a mass balance on the fluid in the gap, $d^2\dot{h} \sim hdu$, we obtain

$$\left(\frac{\dot{h}}{h}\right)_{\mathrm{SEP}} \sim -\frac{1}{1+Ca(a/d)^2}\left(\frac{\dot{h}}{h}\right)_{\mathrm{APP}} - \dot{\gamma}\frac{1}{1+\lambda}\,, \tag{3.2}$$

where the first term on the right-hand side, given by (3.1), describes the increase in gap thickness resulting from capillary suction and suction from the flow that pulls the drops apart. The second term describes film draining that results from the internal circulation convecting fluid out of the gap. Derivation of the above result shows that the pressure in the lubrication gap dominates the pressure inside the drops.

For spherical drops $Ca \ll h/a$ with $d \sim (ah)^{1/2}$, the internal circulation is unimportant. The separation rate predicted by (3.2) reduces to $(\dot{h}/h)_{\mathrm{SEP}} \sim -(\dot{h}/h)_{\mathrm{APP}}$ as expected. However, the behaviour of deformable drops is more complex.

For $Ca > 0$, a distinct flow regime exists at the edge of the flattened near-contact region. The characteristic length of this region is given by the local radius of curvature which is small compared to d. Thus, the flow in this region is dominated by surface tension. Accordingly, the drop interfaces 'peel' apart with the surface-tension-driven velocity $u = \sigma/[\mu(1+\lambda)]$ although the actual velocity is limited by the positions of the drops and therefore cannot exceed $\dot{\gamma}a$. This gives a 'peeling rate':

$$\frac{u}{d} \sim \dot{\gamma}\frac{a/d}{(1+\lambda)Ca+1}.$$

Then combining with (3.2), we obtain the separation rate for closely spaced drops with $Ca > 0$ in the extensional quadrant of a shear flow:

$$\left(\frac{\dot{h}}{h}\right)_{\mathrm{SEP}} \sim \dot{\gamma}\frac{a}{d}\,\frac{1}{(1+\lambda)Ca+1} - \dot{\gamma}\frac{1}{1+\lambda}, \qquad Ca > 0 \tag{3.3}$$

where the first term on the right-hand side describes the drop separation rate that results from peeling of the drop interfaces; the second term on the right-hand side describes film draining that results from internal circulation. The term involving $\left(\dot{h}/h\right)_{\mathrm{APP}}$ has been omitted because it is subdominant as explained below.

From (3.1), the above result, and the estimates provided in table 1, it can be shown that for deformable drops, $\left(\dot{h}/h\right)_{\mathrm{SEP}} \gg \left(\dot{h}/h\right)_{\mathrm{APP}}$. The time scale for drop separation is much shorter than the time scale for their approach. This observation suggests that in the zero deformation limit, deformable drops behave like spherical drops stabilized against coalescence by a singular short-range repulsion. This prediction is supported by the calculations depicted in figures 5 and 7 which indicate that the cross-flow trajectory displacements for $Ca = 0$ are close to those obtained for $Ca = 0.1$ with $\lambda = 1$ and for $Ca = 0.3$ with $\lambda = 20$.

According to (3.3), the opposing effects of interface peeling which promotes drop separation and internal circulation which promotes film drainage are the same order of magnitude for $Ca = O(1)$ and $\lambda = O(1)$. Thus, it is possible for the gap to *thin*

https://doi.org/10.1017/S0022112097005016 Published online by Cambridge University Press

exponentially fast when two closely spaced drops are *pulled apart* by the flow. This unexpected behaviour was observed for calculations with viscosity ratios in the range $2 \leqslant \lambda \leqslant 8$ as depicted in figure 6(*c–e*) in each case, the fourth frame shows the rapid thinning as the two drops are pulled apart. The different role of the outer flow on gap thinning in the compressional and extensional quadrants is affected by the shape and orientation of the isolated drops: lower-curvature portions of the drop surfaces are pressed together in the compressional quadrant; higher-curvature portions are closest when the drops rotate into the extensional quadrant of the flow. For $\lambda < 1$, our numerical calculations indicate that peeling is much faster than drainage.

For $0 < Ca \ll (1+\lambda)^{-2/3}$ ($d \sim a(Ca)^{1/2}$) and for $Ca = O(1)$ with $\lambda \gg 1$ ($d \sim a\lambda^{-1/3}$) equation (3.3) predicts that drop separation is dominated by interface peeling so that the drops separate without film drainage; figure 6(*f*) demonstrates the latter prediction.

3.4. *Drop breakup*

The critical capillary number for breakup of an isolated drop in shear flow is lowest for $\lambda \approx 1$; for $\lambda = 1$, $Ca \approx 0.41$ is critical (Rallison 1981). The trajectory depicted in figure 4(*d*) demonstrates that even for capillary numbers very close to critical, strong pairwise interactions do not result in drop breakup. Other calculations with $\lambda \neq 1$ also showed no tendency for interaction-enhanced breakup. Apparently pairwise drop interactions do not induce significantly subcritical capillary number breakup. Thus, the critical capillary number is a weak function of volume fraction at least in dilute emulsions.

In part, breakup is averted because of the reduced cross-section for interaction between highly deformed drops. Breakup requires enhanced drop elongation but a detailed inspection of the numerical results revealed that the extra deformation induced by a pairwise interaction tends to deform drops in the x_3-direction. Deformable drops can easily squeeze past each other which tends to prevent breakup.

3.5. *Trajectory displacements*

Figures 8 and 9 demonstrate how cross-flow trajectory displacements are affected by drop deformation (shear rate). The grids depicted in figures 8 and 9 are different from those that were used to compute self-diffusivities (cf. §2.4).

Figure 8 shows that trajectory displacements vanish outside a finite initial offset, $R \leqslant 2E_{12}^{1/3}$. Figure 9 reveals the long-range interactions for $Ca > 0$ that result from drop deformation. The results show that for closely spaced trajectories, cross-flow displacements are larger for $Ca = 0.1$; the converse is true for widely spaced trajectories. For $Ca = 0.1$, trajectory displacements with initial offsets $R > 2$ make only a minor contribution to the self-diffusivity but for $Ca = 0.3$, the far-field contribution is about $\frac{1}{3}$. Figure 5 shows that for closely spaced trajectories, displacements tend to decrease with drop deformation, possibly because of the reduced cross-section for near-contact interactions.

Cross-flow trajectory displacements vanish in the smooth hard-sphere limit, $\lambda \to \infty$, as illustrated in figure 7. The results depicted in figure 7 indicate that cross-flow trajectory displacements vary inversely with drop viscosity. For $\lambda = 20$, the cross-flow separation between two drops recovers appreciably after their interaction but only slight recovery occurs for $\lambda = 0.25$; calculations with $\lambda < 0.1$ show essentially no recovery.

https://doi.org/10.1017/S0022112097005016 Published online by Cambridge University Press

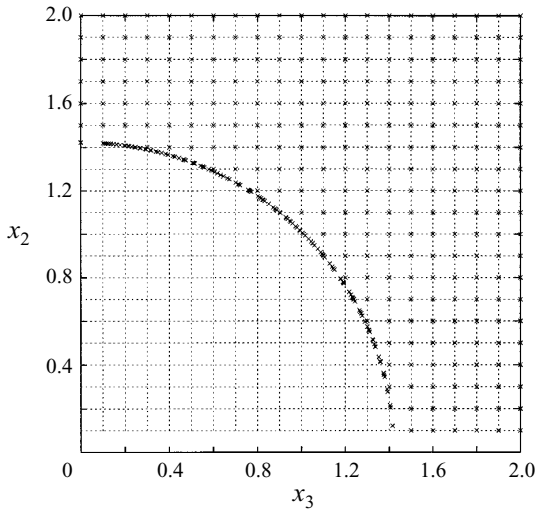


FIGURE 8. Trajectory displacements for $\lambda = 1$, $Ca = 0$. Trajectories originate from $(-20, x_2^0, x_3^0)$, where (x_2^0, x_3^0) are vertices of the light dashed grid. Trajectories terminate at $(+20, x_2, x_3)$, where (x_2, x_3) are marked with $\times$.

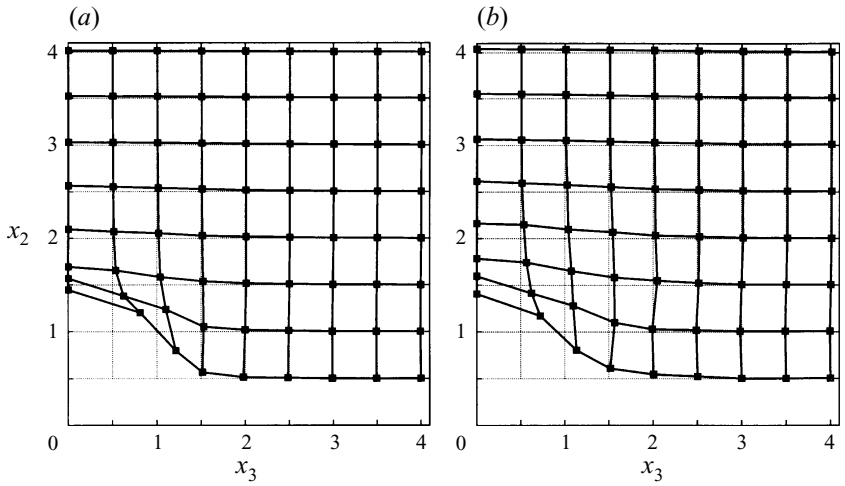


FIGURE 9. Trajectory displacements for $\lambda = 1$: (*a*) $Ca = 0.1$, (*b*) $Ca = 0.3$. Trajectories originate from $(-10, x_2^0, x_3^0)$, where (x_2^0, x_3^0) are vertices of the light dashed grid. Trajectories terminate at $(+10, x_2, x_3)$, where (x_2, x_3) are vertices of the heavy solid grid marked with $\square$.

Inspection of figures 8 and 9 reveals that cross-flow trajectory displacements are considerably biased in the velocity gradient direction rather than the vorticity direction. As a result, drop self-diffusion is anisotropic.

4. Self-diffusivities

Figures 10 and 11 depict self-diffusivities as functions of shear rate (capillary number) and viscosity ratio. The results are accurate to about 2% for deformable drops and about 0.1% for spherical drops. Self-diffusion is only a moderate function of capillary number; figures 10 and 11 show that self-diffusivities vary by a factor

https://doi.org/10.1017/S0022112097005016 Published online by Cambridge University Press

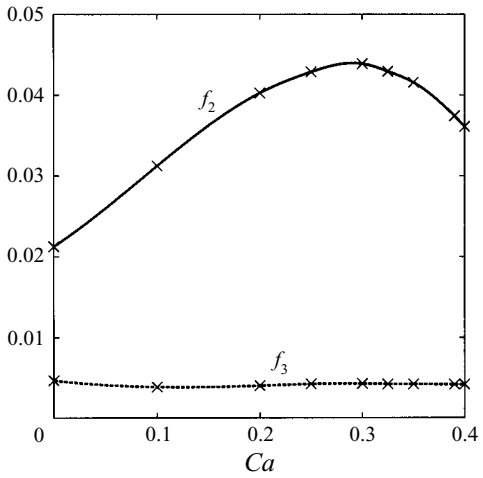


FIGURE 10. Self-diffusion coefficients as a function of capillary number for $\lambda = 1$; solid curve: diffusion parallel to velocity gradient, f_2; dashed curve: diffusion parallel to vorticity, f_3.

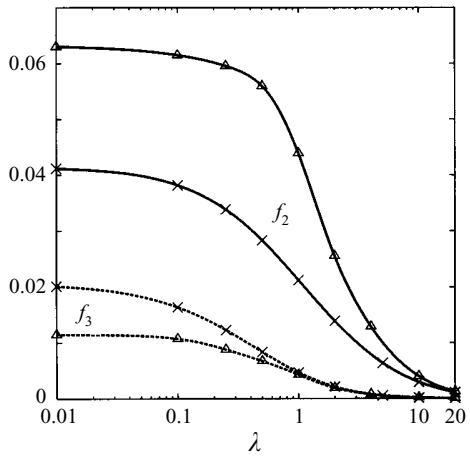


FIGURE 11. Self-diffusion coefficients as a function of viscosity ratio for $Ca = 0.3$ ($\triangle$) and $Ca = 0$ ($\times$); solid curves: diffusion parallel to velocity gradient, f_2; dashed curves: diffusion parallel to vorticity, f_3.

of about 2 as the capillary number is varied over a wide range. By contrast, self-diffusivities are a strong function of viscosity ratio.

Anisotropic self-diffusion results from the bias of trajectory displacements in the velocity gradient direction. Self-diffusion in the velocity gradient direction, f_2, is much larger than self-diffusion in the vorticity direction, f_3. For stabilized spherical bubbles ($\lambda = 0$), the ratio f_2/f_3 is exactly 2 which is a consequence of $B(r, 0) = 0$. For bubbles with $Ca = 0.3$, $f_2/f_3 \simeq 6$. Figure 11 indicates that anisotropy increases with viscosity ratio; $f_2/f_3 > 20$ for $\lambda \geqslant 10$.

For spherical drops with $\lambda = 10$, f_2 and f_3 are approximately equal to the self-diffusivities predicted for spherical particles with 3% roughness (da Cunha & Hinch 1996). For $\lambda < 10$, drop diffusivities are considerably larger than the values for rough spherical particles.

As expected, self-diffusivities vanish for large λ because $D = O(\phi^2)$ for smooth

https://doi.org/10.1017/S0022112097005016 Published online by Cambridge University Press

spheres (Wang *et al.* 1996). The numerical results indicate that self-diffusivities vanish exponentially for $\lambda \gg 1$ with $Ca = 0$. For $\lambda \gg 1$, drop deformation vanishes as $\delta \sim \lambda^{-2/3}$ for $Ca \geqslant \lambda^{-2/3}$ according to the scaling arguments presented in §3.2. This scaling and the results of da Cunha & Hinch (1996) for slightly roughened particles suggests that $f_3 \sim \lambda^{-2/3}$ and $f_2 \sim \lambda^{-0.2916}\left(1.347 + \frac{2}{3}\ln\lambda\right)^{-0.7012}$ for $\lambda \gg 1$ with $Ca > 0$. However, we did not test this prediction with our calculations. The results depicted in figure 11 seem to indicate that self-diffusion becomes insensitive to capillary number for $\lambda \gg 1$.

Figure 10 shows that f_2 exhibits a maximum which may result from a balance between the increase of far-field ($R > 2$) trajectory displacements with drop deformation and the decrease of near-field trajectory displacements with reduced drop cross-section. Under the same conditions, f_3 is essentially independent of Ca. Figure 10 shows a smooth transition from results for $Ca \geqslant 0.1$ to the results for $Ca = 0$ that were obtained using spherical drops stabilized against coalescence by a short-range singular repulsion.

5. Conclusions

Cross-flow self-diffusivities have been computed for drops in a dilute emulsion. Drops have large self-diffusivities compared to rigid spherical particles. For smooth rigid spheres, pairwise interactions are reversible; self-diffusion relies on multiparticle interactions. For deformable drops or sterically stabilized spherical drops, pairwise interactions produce net cross-flow displacements that generate self-diffusion of the drops.

The results show that self-diffusivities depend strongly on the viscosity ratio and moderately on the capillary number. Self-diffusivities are much larger in the velocity gradient direction than in the vorticity direction. The interactions between deformable drops were described with boundary integral calculations; $O(1/N)$ numerical convergence was obtained, where N is the number of boundary elements. Mobility functions for spherical drops were used to describe the interactions between drops in the zero deformation limit.

The coalescence of real drops ($Ca > 0$) requires van der Waals attraction. If $Ca \ll 1$ or $\lambda \neq O(1)$ the *tendency* for coalescence is greatest when drops are pressed together by the shear flow. For a range of order-one viscosity ratios and $Ca = O(1)$, the tendency for coalescence is greatest when closely spaced drops are *pulled apart* in the extensional quadrant of the flow field. For $Ca \ll 1$, drops behave like spherical drops that are stabilized against coalescence by a singular short-range repulsion. These results were obtained by scaling arguments and illustrated by numerical calculations. Further studies are needed to confirm these predictions. In particular, more detailed calculations are needed to resolve the complex behaviour that occurs when deformable drops separate.

The calculations also indicate that drop interactions do not induce significantly subcritical capillary number breakup. In dilute emulsions, the critical capillary number is a weak function of volume fraction because deformable drops can easily squeeze past each other.

The authors thank Dr John Rallison for help with the scaling arguments presented in §3.2–3.3. The authors thank Dr Alexander Zinchenko for his FORTRAN subroutines that compute the mobility functions for spherical drops.

M.L. was supported in part by a NATO-NSF Fellowship, in part by NASA

https://doi.org/10.1017/S0022112097005016 Published online by Cambridge University Press

grant NAG3-1935, and in part by NSF grant CTS-9624615. The computations were supported in part by the SERC CSI grant GR/H57585, the DTI LINK programme on colloids, NASA grant NAG3-1935, and NSF grant CTS-9624615.

REFERENCES

Brady, J. F. & Bossis, G. 1987 Self-diffusion of particles in concentrated suspensions under shear. *J. Chem. Phys.* **87**, 5437–5448.

Chesters, A. K. 1991 The modelling of coalescence processes in fluid-liquid dispersions: a review of current understanding. *Trans. Instn Chem. Engrs* **69**, 259–270.

Cunha, F. R. da & Hinch, E. J. 1996 Shear-induced dispersion in a dilute suspension of rough spheres. *J. Fluid Mech.* **309**, 211–223.

Davis, R. H., Schonberg, J. A. & Rallison, J. M. 1989 The lubrication force between two viscous drops. *Phys. Fluids A* **1**, 77–81.

Eckstein, E. C., Bailey, D. G. & Shapiro, A. H. 1977 Self-diffusion of particles in shear flow of a suspension. *J. Fluid Mech.* **79**, 191–208.

Grace, H. P. 1971 Dispersion phenomena in high viscosity immiscible fluid systems and application of static mixers as dispersion devices in such systems. *Eng. Found., Res. Conf. Mixing, 3rd, Andover, NH* (republished 1982 in *Chem. Engng Commun.* **14**, 225–277).

Hinch, E. J. & Acrivos, A. 1980 Long slender drops in a simple shear flow. *J. Fluid Mech.* **98**, 305–328.

Leighton, D. T. & Acrivos, A. 1987 Measurement of shear-induced self-diffusion in a concentrated suspension of spheres. *J. Fluid Mech.* **177**, 109–131.

Loewenberg, M. & Hinch, E. J. 1996 Numerical simulation of a concentrated emulsion in shear flow. *J. Fluid Mech.* **321** 395–419.

Pozrikidis, C. 1992 *Boundary Integral and Singularity Methods for Linearized Viscous Flow*. Cambridge University Press.

Rallison, J. M. 1981 A numerical study of the deformation and burst of a drop in general shear flows. *J. Fluid Mech.* **109**, 465–482.

Wang, H., Zinchenko, A. Z. & Davis, R. H. 1994 The collision rate of small drops in linear flow fields. *J. Fluid Mech.* **265**, 161–188.

Wang, Y., Mauri, R. & Acrivos, A. 1996 The transverse shear-induced liquid and particle tracer diffusivities of a dilute suspension of spheres undergoing a simple shear flow. *J. Fluid Mech.* **327**, 255–272.

Yiantsios, S. G. & Davis, R. H. 1991 Close approach and deformation of two viscous drops due to gravity and van der Waals forces. *J. Colloid Interface Sci.* **144**, 412–433.

Zinchenko, A. Z. 1982 Effect of hydrodynamic interactions between the particles on the rheological properties of dilute emulsions. *Prikl. Mat. Mech.* **46**, 72–82.

Zinchenko, A. Z. 1983 Effect of hydrodynamic interactions between the particles on the rheological properties of dilute emulsions. *Prikl. Mat. Mech.* **47**, 56–63.

Zinchenko, A. Z. 1984 Effect of hydrodynamic interactions between the particles on the rheological properties of dilute emulsions. *Prikl. Mat. Mech.* **48**, 198–206.

https://doi.org/10.1017/S0022112097005016 Published online by Cambridge University Press